



OPEN ACCESS

EDITED BY

Francesca Altieri,
Institute for Space Astrophysics and
Planetology (INAF), Italy

REVIEWED BY

Alice Le Gall,
Université de Versailles
Saint-Quentin-en-Yvelines, France
Jianguo Yan,
Wuhan University, China

*CORRESPONDENCE

Jinhai Zhang,
✉ zjh@mail.iggcas.ac.cn

RECEIVED 17 March 2023

ACCEPTED 14 June 2023

PUBLISHED 28 June 2023

CITATION

Lv W and Zhang J (2023),
High-resolution permittivity estimation
of ground penetrating radar data by
migration with isolated hyperbolic
diffractions and local focusing analyses.
Front. Astron. Space Sci. 10:1188232.
doi: 10.3389/fspas.2023.1188232

COPYRIGHT

© 2023 Lv and Zhang. This is an
open-access article distributed under
the terms of the [Creative Commons
Attribution License \(CC BY\)](https://creativecommons.org/licenses/by/4.0/). The use,
distribution or reproduction in other
forums is permitted, provided the
original author(s) and the copyright
owner(s) are credited and that the
original publication in this journal is
cited, in accordance with accepted
academic practice. No use, distribution
or reproduction is permitted which does
not comply with these terms.

High-resolution permittivity estimation of ground penetrating radar data by migration with isolated hyperbolic diffractions and local focusing analyses

Wenmin Lv^{1,2,3,4} and Jinhai Zhang^{1,2,3,4*}

¹Engineering Laboratory for Deep Resources Equipment and Technology, Institute of Geology and Geophysics, Chinese Academy of Sciences, Beijing, China, ²Key Laboratory of Earth and Planetary Physics, Institute of Geology and Geophysics, Chinese Academy of Sciences, Beijing, China, ³Innovation Academy for Earth Science, Chinese Academy of Sciences, Beijing, China, ⁴College of Earth and Planetary Sciences, University of Chinese Academy of Sciences, Beijing, China

Ground penetrating radar (GPR) is important for detecting shallow subsurface structures, which has been successfully used on the Earth, Moon, and Mars. It is difficult to analyze the underground permittivity from GPR data because its observation system is almost zero-offset. Traditional velocity analysis methods can work well with separable diffractions but fail with strong-interfered diffractions. However, in most situations, especially for lunar or Martian exploration, the diffractions are highly interfered, or even buried in reflections. Here, we proposed a new method to estimate the underground permittivity and apply it to lunar penetrating radar data. First, we isolate a group of diffractions with a hyperbolic time window determined by a given velocity. Then, we perform migration using the given velocity and evaluate the focusing effects of migration results. Next, we find the most focused results after scanning a series of velocities and regard the corresponding velocity as the best estimation. Finally, we assemble all locally focused points and derive the best velocity model. Tests show that our method has high spatial resolution and can handle strong noises, thus can achieve velocity analyses with high accuracy, especially for complex materials. The permittivity of lunar regolith at Chang'E-4 landing area is estimated to be ~4 within 12 m, ranging from 3.5 to 4.2 with a local perturbation of ~2.3%, consistent with ~3% obtained by numerical simulations using self-organization random models. This suggests that the lunar regolith at Chang'E-4 landing area is mature and can be well described by self-organization random models.

KEYWORDS

ground penetrating radar, diffraction isolation, migration, Moon, chang'E-4

1 Introduction

Ground penetrating radar (GPR) is important for detecting shallow subsurface structures, which has been successfully used on the Earth, Moon, and Mars (Boisson et al., 2009; Jordan et al., 2009; Fang et al., 2014; Xiao et al., 2015; Zhang et al., 2015; Schroeder et al., 2019; Hamran et al., 2020; Zhou et al., 2020; Oudart et al., 2021; Zhang X et al., 2021; Li et al., 2022). However, it is difficult to analyze the underground

velocity because the observation system of the GPR is almost zero-offset (i.e., the transmitter and the receiver are close to each other in position), which has no enough number of multiple offsets (Su et al., 2014; Zhang et al., 2014; Fa et al., 2015; Feng et al., 2019). Consequently, we can only estimate the velocity using methods originally developed for zero-offset data (Economou et al., 2020; Leong and Zhu, 2021). Fortunately, the zero-offset radar profiles are similar to the post-stack seismic profiles; thus, we can take the benefits of the velocity estimation methods that were developed in seismic exploration field for post-stack seismic profiles (Claerbout, 1985; Zhu et al., 1998; Hu et al., 2001; Fomel et al., 2007; Reshef and Landa, 2009; Carpentier et al., 2010).

The simplest method of velocity estimation is to assign a constant velocity for each identifiable layer, assuming that there is no lateral variation in each layer (Dai et al., 2014; Li et al., 2017). Undoubtedly, this method would encounter great uncertainty because it is difficult to evaluate the accuracy of velocity estimations. Another velocity estimation method is to fit hyperbolic-shape diffractions in the GPR profiles by velocity scanning (Yilmaz, 2001; Ristic et al., 2009; Dong et al., 2020; Giannakis et al., 2021). However, this method requires that the diffractions have a relatively high signal-to-noise ratio and have little interference from adjacent hyperbolas. In the presence of strong scattering, the diffractions from different objects mostly gather together rather than staying isolated; thus, it is difficult to separate them with existing methods.

Another method of velocity analysis is to focus the diffractions by migration (Sava et al., 2005; Yuan et al., 2019). The migration-based methods can numerically collect the weak diffractions into smaller areas and undoubtedly enhance the local signal-to-noise ratio in the migration domain (Li and Zhang, 2022a); however, the available amount of diffractions for this method is relatively limited; consequently, we can not cover the whole model and leave some empty regions, especially in the presence of strongly cluttered diffractions. Unfortunately, this is the usual case for the Moon and Mars, because the extraterrestrial bodies had experienced long-term impact. The abundant ejecta in subsurface layers would cause strong interference of diffractions in the GPR data. Therefore, many existing velocity analysis methods can achieve good results for theoretical models with sparse scattering objects but are almost powerless for models with vast strong-scattering objects.

The diffraction separation technique was proposed in seismic exploration field for zero-offset data (Fomel, 2003a; Fomel, 2003b). This method performs plane wave decomposition-based local curvature analysis to separate diffractions from reflections. However, as a data-driven method, it relies on curvature analysis in the data domain (Fomel et al., 2007; Li et al., 2021a; Song et al., 2021; Li and Zhang, 2022b) and is vulnerable to the influence of the original signal-to-noise ratio. Additionally, all rapid local variations of curvature tend to be regarded as diffractions, while the others are regarded as reflections. Thus, the reflections and diffractions can not be fully separated purely by local variations of curvature, since some reflections may also have relatively rapid local variations of curvature and the diffractions may also have relatively slow local variations of curvature. Therefore, new methods on GPR velocity analyses are needed to identify weak diffractions precisely and avoid the interferences from both adjacent diffractions and strong reflections.

In this paper, we proposed a new method to estimate the permittivity (converted from velocity) of subsurface materials based on migration and diffraction isolation. First, we isolate a group of diffractions in the un-migrated domain with hyperbolic windows determined by a given velocity. Then, we perform migration on the isolated data using the given velocity and evaluate the focusing effects of the migration results of isolated diffractions. Next, we pick up the most focused results after scanning a series of velocities and regard the corresponding velocity as the best estimation. Finally, we obtain a dense set of velocity estimation points at all locally focused positions, and the best estimation of the velocity model can be derived after assembling all available points.

2 Methodology

In this section, we show the details of the proposed method for estimating the permittivity of subsurface materials (Figure 1). There are three steps: 1) isolating weak diffractions with a set of hyperbolic windows determined by different velocities; 2) collecting the isolated weak diffractions by migration; 3) focusing analysis by evaluating the ratio of amplitudes between the focused point and around the focused point in the migrated domain.

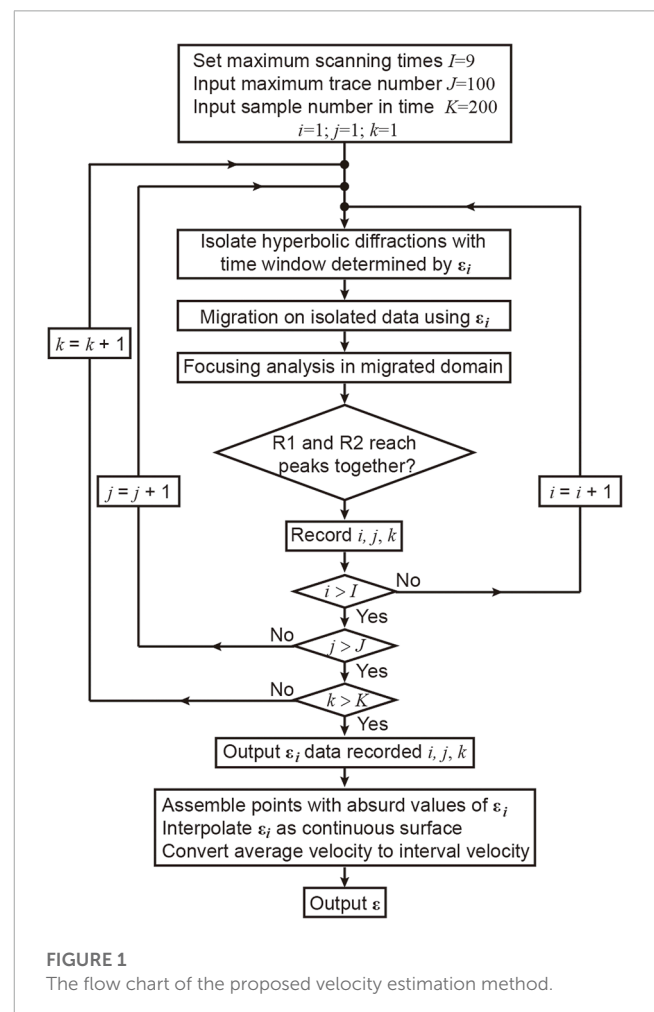


FIGURE 1
The flow chart of the proposed velocity estimation method.

The permittivity of lunar regolith and basalt blocks generally ranges from 3 to 7 (Olhoeft et al., 1975a; Heiken et al., 1991). Within this range, we apply grid searching on nine possible values. In the migrated domain, we define two parameters to evaluate the focusing effects under a given velocity, and the diffractions can be easily identified from cluttered diffractions and reflections.

2.1 Formation of hyperbolic-shape diffractions in GPR profile

The electromagnetic wave can propagate in the air and underground media. We can observe back-propagating waves of reflections on the boundary of diffractors with discontinuous dielectric properties, such as basalt blocks (Hiesinger and Head, 2006; Jolliff et al., 2006; Fa et al., 2015); similarly, we can also observe diffractions when the size of diffractor is comparable to the wavelength of electromagnetic wave. The energy of diffractions is usually smaller than that of the reflections.

We assume that each block of ejecta or rocks can be considered as a point-like diffractor since the influence of scattering body decreases with the increase of depth h_0 (m); thus, the travel time of diffractions presents as a hyperbola in the GPR profile (Capineri et al., 2008; Ristic et al., 2009; Kouemou, 2010; Soldovieri and Solimene, 2010; Ding et al., 2020; Lv et al., 2020), when the GPR rover moving from x to x_0 over the diffractor at (x_0, h_0) . Figure 2A illustrates the forming principle and geometric relationship of corresponding diffractions as

$$(x_0 - x)^2 + h_0^2 = v^2 t^2, \quad (1)$$

which can be transformed into a hyperbolic form as

$$\frac{t^2}{\left(\frac{h_0}{v}\right)^2} - \frac{(x_0 - x)^2}{h_0^2} = 1, \quad (2)$$

where t represents the one-way travel time, v represents the average propagating velocity of electromagnetic waves. Given the location of a scatterer at (x_0, h_0) , the only parameter controlling the shape

of hyperbola will be v . The relative magnetic permeability of most subsurface material approximately equals to 1 and the conductivity affects little during the wave propagation for high-frequency radar waves; thus, the media could be regarded as ideal dielectric and v can be calculated by (Heiken et al., 1991)

$$v = \frac{c}{\sqrt{\epsilon_r}}, \quad (3)$$

where c is the speed of light in vacuum and ϵ_r is the relative dielectric permittivity (Gold et al., 1972; Olhoeft et al., 1974; Heiken et al., 1991; Rochette et al., 2010). At the same location, for a smaller permittivity, the propagating velocity will be higher and the corresponding hyperbola will be sharper and narrower; in contrast, for a larger permittivity, the velocity will be lower and the corresponding hyperbola will be flatter and broader (Figure 2B).

2.2 Improving signal-to-noise using migration

Migration is a common technique for imaging underground structures (Claerbout, 1985; Leuschen and Plumb, 2001; Stuart, 2003; Özdemir et al., 2014). It can numerically collect a group of diffractions into a small region around the apex if the permittivity used is close to the true one; as a result, the diffractions originally hidden by strong noises can be highlighted in the migrated domain (Li and Zhang, 2022a; Li and Zhang, 2022b). Here, we use F-K migration (Stolt, 1978), which is a direct method that is the fastest known migration technique.

We test on two simple models with strong random noises to illustrate the necessity of migration on improving signal-to-noise in the migration domain (Figure 3). We can see that the hyperbolic-shape diffractions are almost completely hidden in background noises before using migration. In contrast, the results after using migration (Stolt, 1978) show a clear peak in the wiggle along the apex of diffractions. This indicates that the weak diffractions can be extracted from the strong background noises using migration. In other words, the diffractions can be

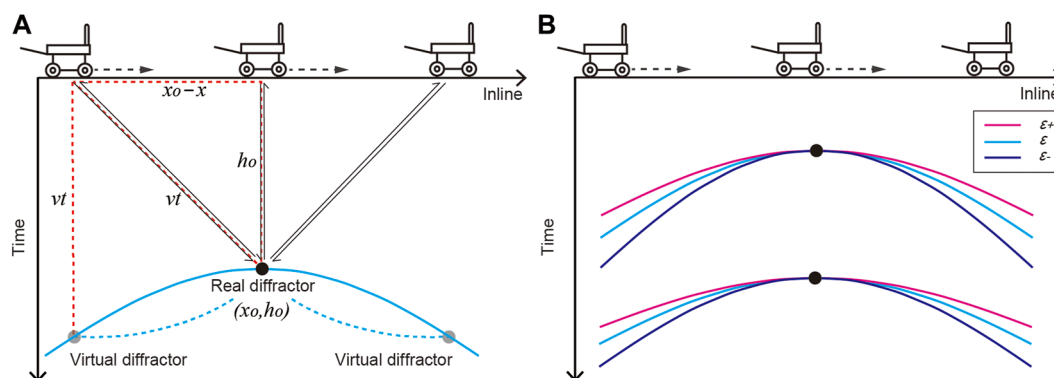


FIGURE 2

Illustration of the generation of diffractions and their isolations. (A) Mechanism of the radar observation and the forming principle of diffractions. The black lines with arrows indicate the propagation tracks of electromagnetic waves, the blue hyperbola represents the corresponding echo from the point-like diffractor in the radargram. (B) The center hyperbolas of isolating windows determined by different permittivities.

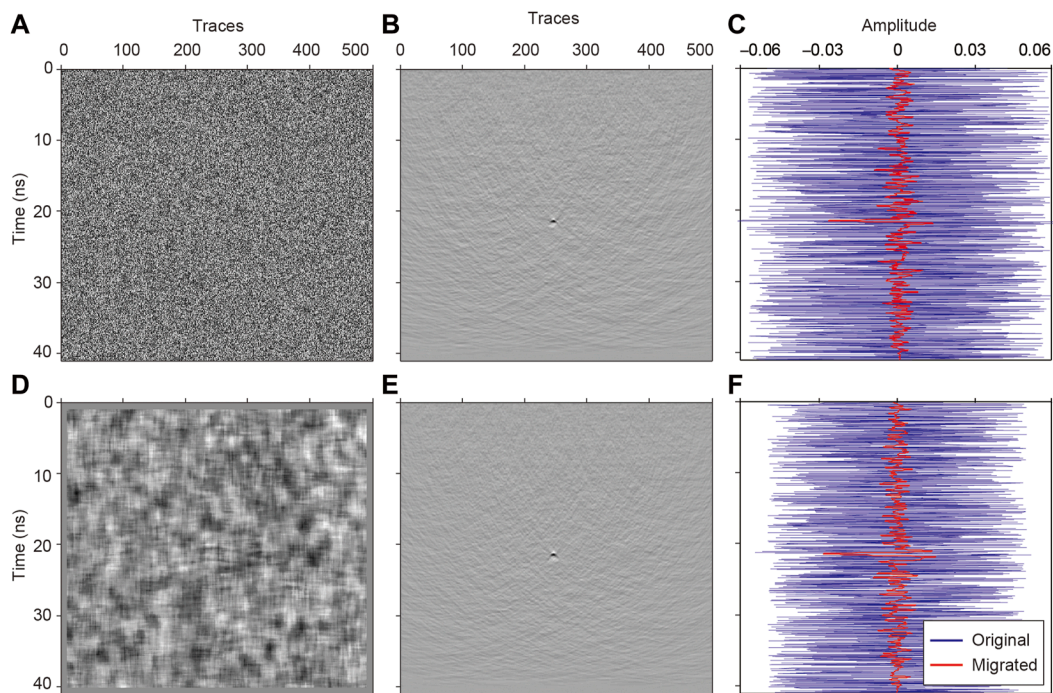


FIGURE 3

Illustration of improving the signal-to-noise ratio using migration. (A) Weak hyperbolic-shape diffractions buried in strong random noises. (B) The migration results of (A). (C) Comparison of wiggles of the one trace along the apex of diffractions: the blue curve denotes the original data shown in (A) and the red curve denotes the migrated profile shown in (B). (D–F) Another case similar to (A–C) but with a different kind of random noises shown in (D).

highlighted after migration and the energy peak can well indicate the location of the diffractor. With migration, we can achieve the best velocity estimation after comparing the focusing effects under different velocities. However, the actual media is far more complex with a large number of scattering objects; additionally, their diffractions mostly gather together and interfere with each other, especially for the widely existing ejecta layer on the Moon and Mars. Thus, the velocity analyses after directly using migration could not well separate these interferences. We propose to generate a series of hyperbola windows within the possible range of permittivity to isolate each group of diffractions and suppress both random noises and the interferences. The velocity analyses are performed on these isolated data thus can well handle cluttered diffractions.

2.3 Diffraction isolation

The isolation of diffractions and the migration had been proven effective in reducing the above-surface diffractions (Li et al., 2021a). Traditional methods perform migration to the whole data set without isolating each group of diffractions; thus, the cluttered diffractions are still strongly interfered in the migrated domain (Carpentier et al., 2010). In contrast, we isolate the target diffractions from others in the un-migrated domain by some proper windows, which can largely avoid the influence from both adjacent diffractions and reflections, since the input data for the migration are dominated by the target diffractions and only small parts of

adjacent diffractions or some segments of reflections exist. This can greatly improve the signal-to-noise ratio after applying migration to such windowed input data, compared with applying migration to the whole data; additionally, it can also improve the spatial resolution by separately analyzing each group of diffractions at a time.

According to the forming principle of diffractions, the isolation window can be automatically built up with the widen of the theoretical hyperbola. Therefore, we can build a series of hyperbola windows in different shapes at different depths using various permittivities (i.e., velocities). After analyzing some typical GPR data, we set the temporal width of the window to be 10–20 samples. These windows would be applied to isolate the diffractions from the GPR profile independently, and the surrounding noises and interferences can be well suppressed (Figure 4). In this way, the input data d can be divided into two parts: $d_{w(\epsilon_i)}$ is the isolated part within the hyperbolic window region, the shape of the hyperbolic window is under the control of permittivity ϵ_i , and the rest part is out of the window $d_r = d - d_{w(\epsilon_i)}$.

The main drawback of the proposed method is the huge computational cost, due to dealing with a vast number of potential diffractions independently. Fortunately, the total computational cost becomes affordable after applying a series of optimization steps. First, we apply grid searching on every 5 time steps, this can improve the efficiency greatly while preserving the shapes of diffractions; then, we apply migration within a small region instead of the

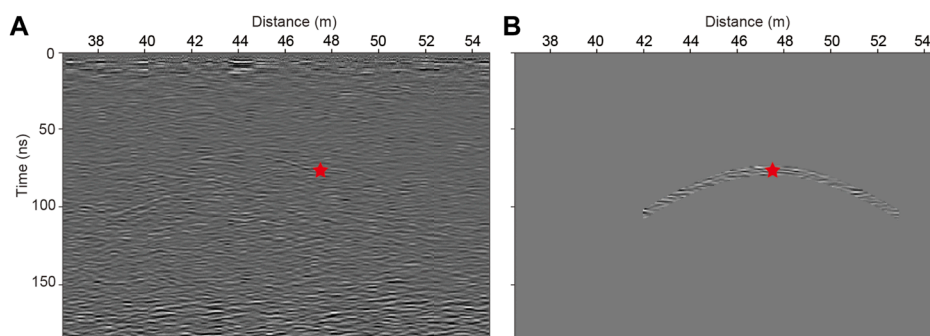


FIGURE 4

Illustration of diffraction isolation in Chang'E-4 LPR profile. (A, B) are the radar profile before and after diffraction isolation, respectively.

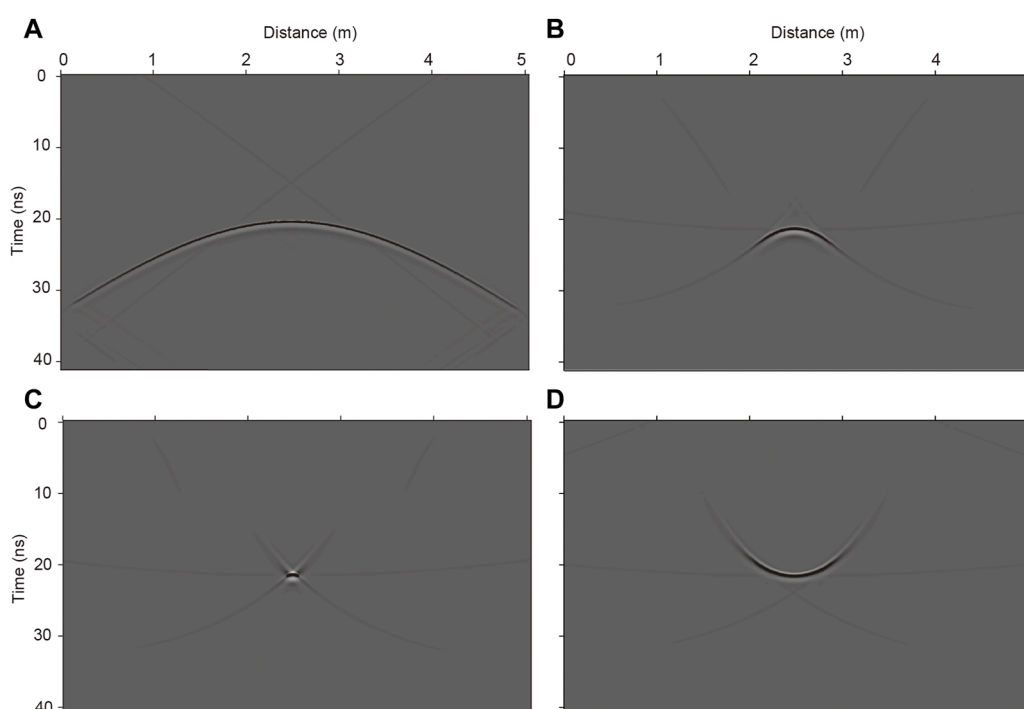


FIGURE 5

Migration results under different permittivities. (A) Hyperbolic-shape diffraction. (B–D) The corresponding migration results with the permittivity of $\epsilon+$, ϵ , and $\epsilon-$, respectively.

whole profile, which can further reduce the computational cost; finally, we adopt a fast implementation of migration (e.g., Stolt, 1978).

2.4 Focusing analyses in migrated domain

For each group of diffractions, permittivity is the key parameter controlling the focusing effects of migration results. If the permittivity is true, the diffractions can be perfectly focused within a small region close to the true location of the diffractor; if too large, the diffractions will be under-migrated and display as a downward-opening curve with reduced spatial scale; otherwise, if

too small, the diffractions will be over-migrated and display as an upward-opening curve (Figure 5) (Claerbout, 1985; Zhu et al., 1998; Li et al., 2021b). For a given group of diffractions, there must be a permittivity model with which the diffractions can be best tailored by a hyperbola window, and the migration results would be highly focused with the highest signal-to-noise ratio. In other words, for a properly-tailored group of diffractions, the permittivity can be determined once we obtain the best-focused migration results. This allows us to finely tune the velocity for each potential diffractor independently.

We assume that one group of diffractions is already tailored properly with a group of given windows determined by the

permittivity ϵi , and A is the migrated result as below

$$A = FKMig(d_{w,\epsilon i}). \tag{4}$$

Then we calculate the partial derivatives H_t and H_x of A in time and horizontal direction,

$$[H_t, H_x] = gradient(A). \tag{5}$$

We then use the sum of H_t and H_x to represent the amplitude variation at point (t_0, x_0) in A , which can be calculated as

$$H(t_0, x_0) = |H_t(t_0, x_0)| + |H_x(t_0, x_0)|. \tag{6}$$

To further quantify the amplitude variation (i.e., the focusing effects around this point under a specific permittivity), we design a gradient template around the target. We bring in a parameter P to express the focusing energy around the target:

$$P = \sum_{t=t_0-u}^{t_0+u} \sum_{x=x_0-v}^{x_0+v} H(t, x), \tag{7}$$

where u and v ($u > 1, v > 1$) represent the side lengths of the template in time and horizontal direction, respectively. Usually, P would be greatly higher for diffractors, compared with non-diffractors. When P exceeds a certain threshold, we consider that there may be diffractors there, which require further focusing analysis. Then we introduce A, B, C, D to represent the focusing energy around the point (t_0, x_0) (Figure 6),

$$A = \sum_{t=t_0-2u}^{t_0-u-1} \sum_{x=x_0-v}^{x_0+v} H(t, x), \tag{8}$$

$$B = \sum_{t=t_0+u+1}^{t_0+2u} \sum_{x=x_0-v}^{x_0+v} H(t, x), \tag{9}$$

$$C = \sum_{t=t_0-u}^{t_0+u} \sum_{x=x_0-2v}^{x_0-v-1} H(t, x), \tag{10}$$

$$D = \sum_{t=t_0-u}^{t_0+u} \sum_{x=x_0+v+1}^{x_0+2v} H(t, x), \tag{11}$$

In different radar profiles with different time step and spatial interval, we need to set different u and v . Figure 6 shows the template under $u = 4, v = 2$. For high-frequency radar profile, u is usually greater than 10 and there will be a multiple difference between u and v . Therefore, we can ignore the effects of signal energy within the gray area in Figure 6 during focus evaluation.

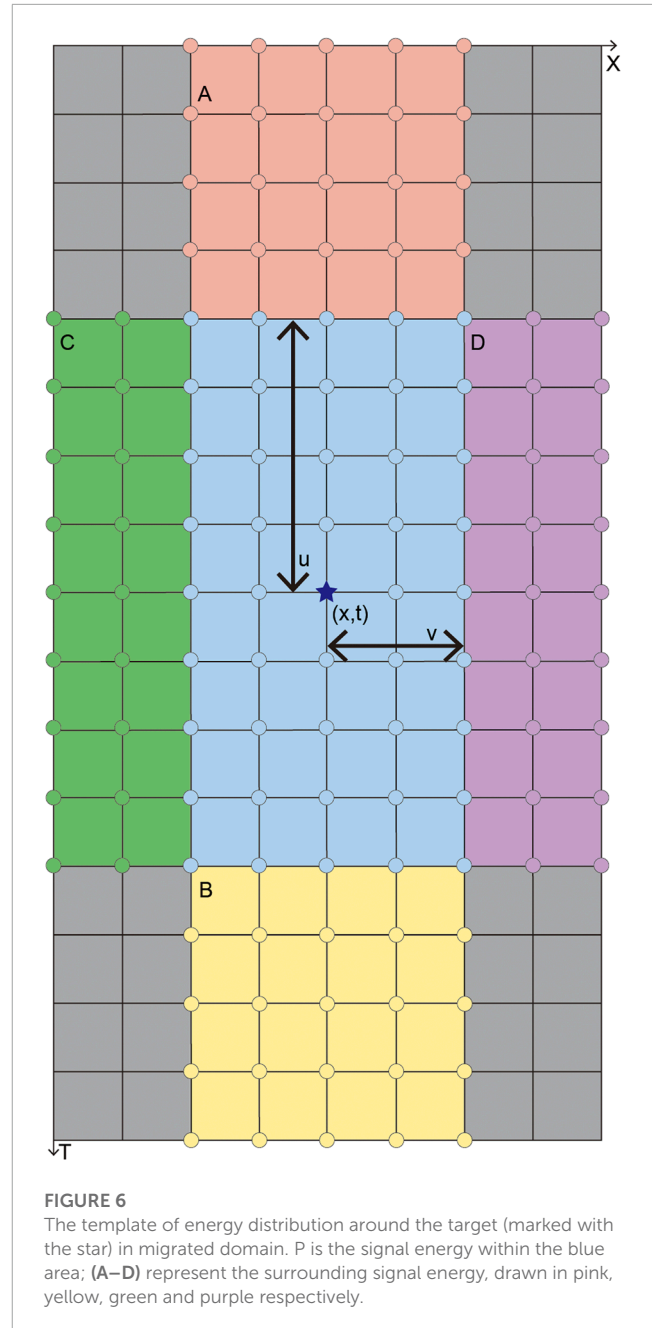
Then we introduce two parameters R_1 and R_2 :

$$R_1 = \frac{P}{P + A + B + C + D}, \tag{12}$$

which is the gradient ratio between the amplitudes of target area (blue region in Figure 6) and all points within the template.

$$R_2 = \frac{P}{A + B + C + D}, \tag{13}$$

which is the gradient ratio between the amplitudes of target area and area around the target (pink, yellow, green and purple region



in Figure 6). These two ratios (i.e., R_1 and R_2) can well represent the focusing effects in the migrated domain.

Here we show the R_1 and R_2 (Figure 7) calculated from Figures 5B–D. It is obvious that the focusing energy is the strongest under an accurate velocity model.

We argue that if there is a diffractor, there must be two maximums of R_1 and R_2 after comparing a series of these two ratios obtained under different permittivities. In other words, when R_1 and R_2 reach their maximums under the same permittivity simultaneously, this permittivity can be regarded as the best estimation; otherwise, we suppose that there is no diffractor at current point. In this way, we can locate the diffractor and estimate the corresponding permittivity simultaneously.

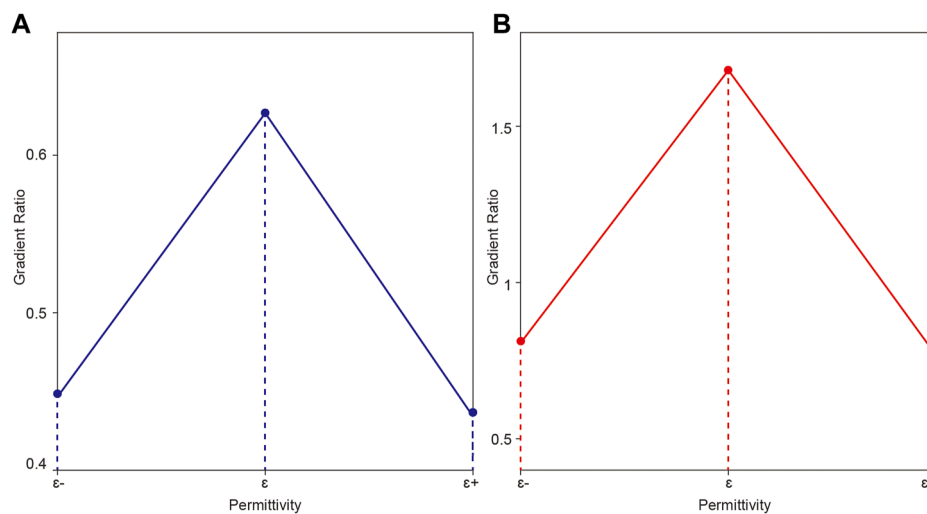


FIGURE 7

Histograms of R1[blue line in 7(A)] and R2[red line in 7(B)]. ϵ^- , ϵ and ϵ^+ corresponds to the over-migrated, perfectly migrated and under-migrated situation, respectively.

3 Application in lunar penetrating radar data

We hope to employ our method to a local lunar penetrating radar (LPR) profile from Chang'E-4 mission (Zhang J et al., 2021), so that we can acquire the corresponding permittivity profiles at the landing site. This can help us to better understand the structure and property of lunar subsurface material.

The LPR onboard Yutu-2 rover has two channels, with the dominant frequency of 60 MHz (Channel-1) and 500 MHz (Channel-2), respectively. We only consider the high-frequency channel, which is for detecting shallow structures. Under the dominant frequency of 500 MHz, the diffractors with diameter over ~15 cm would be mostly identified (Jol., 2009). The Channel-2 antennas are 30 cm over the surface, in Bowtie shape. The two receiving antennas (A and B) are close to the emitter with a distance of 15.4 cm and 31.7 cm, respectively (Fang et al., 2014). The time step of channel 2B is 0.3125 ns and spatial interval is 3.65 cm.

We first test our method with a numerical model to show its feasibility. We build a simple scattering model and perform numerical simulation with the finite-difference method (Figures 8A, B). Based on the simulated radar records, we further carry out the F-K migration and focusing analysis in the migrated domain. The scanning region (the box in Figure 8B) is between 13 ns and 17.7 ns in time, from $x = 0.5$ m to $x = 4.25$ m. Figure 8C shows that our proposed method can well locate the diffractors and derive the corresponding permittivities from the radar record.

3.1 Application in a typical group of diffractors

After confirming the feasibility of this method, we then employ it to a typical group of diffractors from the LPR profile and

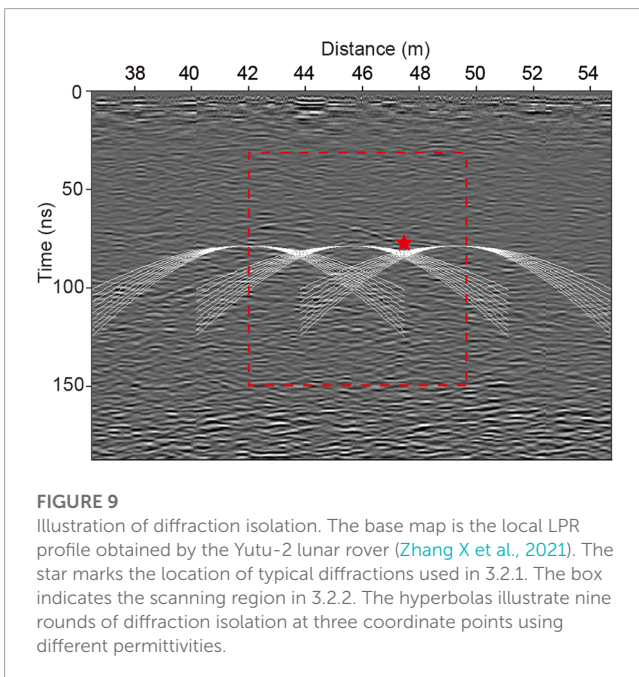
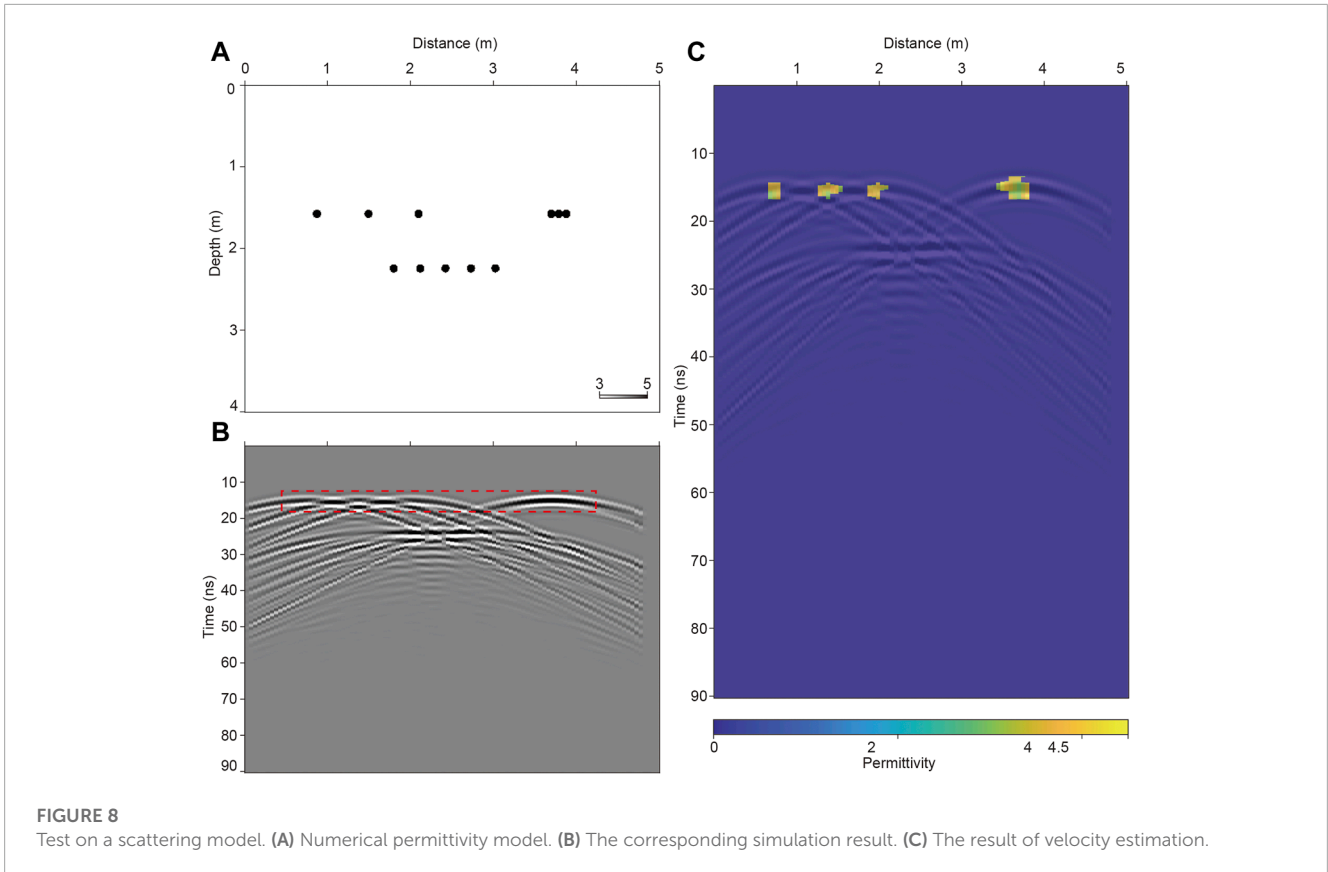
compare the focusing effects in the migrated domain before and after diffraction isolation. The location of the group of diffractors is marked with the red star in Figure 9.

After nine rounds of diffraction isolation and migration, we can obtain nine groups of gradient ratios R1 and R2 (Figures 10A, C). It can be seen that R1 and R2 reach their maximums simultaneously with the permittivity of 4. To be more precise, we refine the permittivity from 3.5 to 4.5 by a one-fifth interval and find that the largest ratios appear at permittivity of 3.7 (Figures 10B, D). Therefore, the best estimation of the permittivity at this point should be 3.7. Under this permittivity, we compare the focusing effects in the migrated domain with or without diffraction isolation (Figure 11). Obviously, the signal energy is better focused after using diffraction isolation, although the peak is slightly reduced compared with that before using diffraction isolation. This indicates that the diffraction isolation can well suppress the interference from noises and surrounding diffractors, which can also explain why the energy peak falls slightly. Besides, the location of the diffractor can be more accurate after diffraction isolation, as shown by the wiggles in Figure 11D.

3.2 Application in local profile

We further apply our method to the local LPR profile. The location of the scanning region is indicated with the red dotted box in Figure 9. The original LPR data have a time step of 0.3125 ns and a spatial interval of 3.65 cm. We pick up the data every 5 time steps from traces No. 1150 to No. 1350 to save the computational cost. Comparing the gradient ratios of R1 and R2, we can pick up the diffractors while recording their corresponding permittivities. Ultimately, we can acquire a two-dimensional map of permittivity distribution using the proposed method (Figure 12).

The depth of the region (red box in Figure 9) is within 20 m, the permittivity is generally between 3 and 5 (Li et al., 2021b).



Therefore, the permittivity beyond the range [3,5] would be absurd. We eliminate the absurd values of permittivity to avoid potential influence from few wild points (Figure 12A). Then we interpolate the permittivity profile to generate continuous velocity estimation

along the whole LPR profile then apply two rounds of median filtering to smooth the interpolated results. It should be noted that the permittivity calculated above represents the depth-averaged permittivity between the surface and the diffractor, instead of the interval permittivity at a specific depth. Thus, we need to transfer it into the interval velocity with Dix inversion as follows (Dix, 1955; Bradford and Harper, 2005; Sato and Feng, 2005)

$$v_{int,t_n} = \sqrt{\frac{v_{ave,t_n}^2 t_n - v_{ave,t_{n-1}}^2 t_{n-1}}{t_n - t_{n-1}}}, \quad (14)$$

where t_n represents the time samples, v_{int,t_n} represents the interval velocity at the time point of t_n , and v_{ave,t_n} represents the average velocity within time t_n , which is the average of the first n temporal pixels. Thus, the interval permittivity can be calculated point by point. Finally, the two-dimensional map of permittivity distribution can be obtained, as shown in Figure 12D. The spatial resolution can be roughly up to 30 cm, comparable to the spatial resolution of the LPR (~30 cm). From Figures 12A, D clear increasing tendency of permittivity versus time can be seen, revealed as an expanded yellow region.

Based on this local map of permittivity distribution, we can gather more information on dielectric property by analyzing the statistical characteristics of lunar regolith. Figure 13A shows the relative permittivity scatterplot derived from the map. The permittivities vary in a similar tendency between different traces, which indicates that there is slight lateral variation along the LPR profile. Additionally, the permittivities on all points are generally ~4 from 30 to 150 ns. The linear fitting results show a tiny increasing

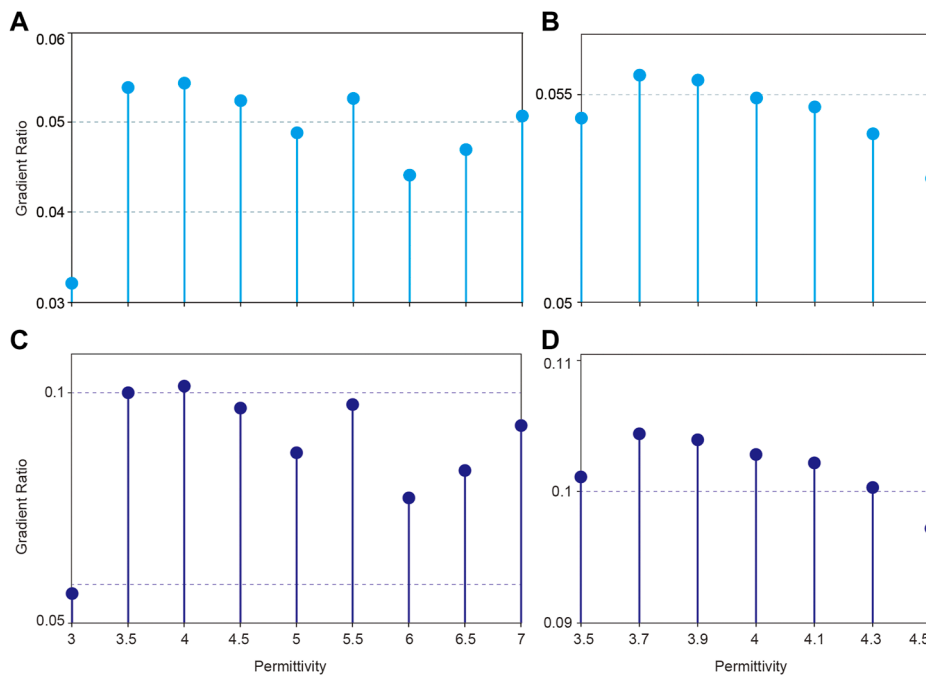


FIGURE 10
The gradient ratios histograms in typical diffraction tests. (A) and (C) list R1 and R2 calculated using different permittivities ranging from 3 to 7, respectively. (B, D) are the locally refined results between 3.5 and 4.5 of (A, C), respectively.

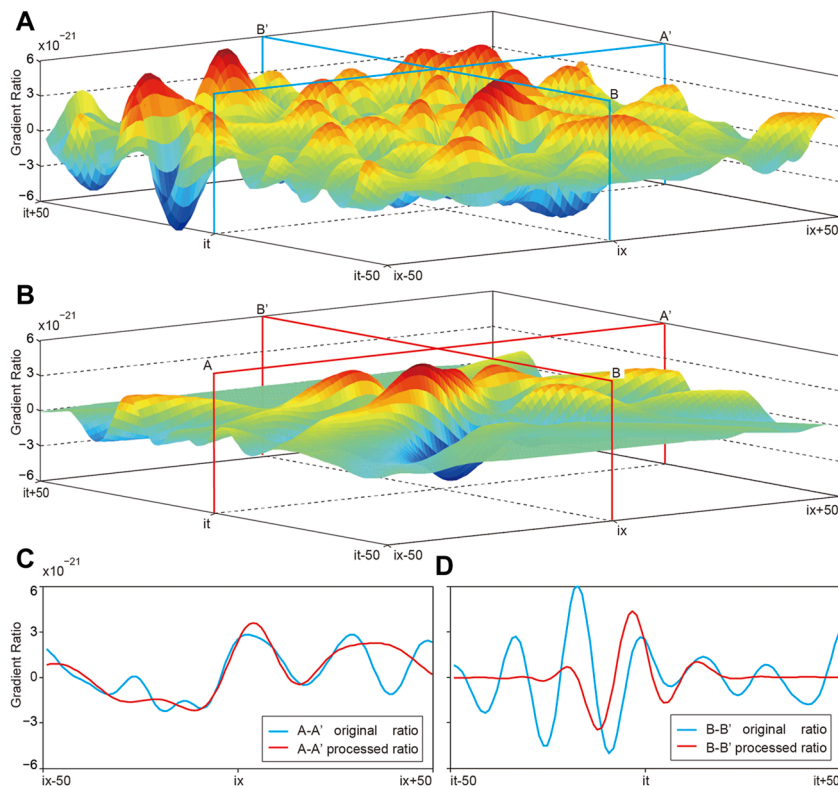


FIGURE 11
Local energy maps and slices of migration. (A, B) are energy maps with or without diffraction isolation, respectively. (*it*, *ix*) is the coordinate of the diffractor. (C) The energy slices along A-A' shown in (A, B). (D) The energy slices along B-B' shown in (A, B).

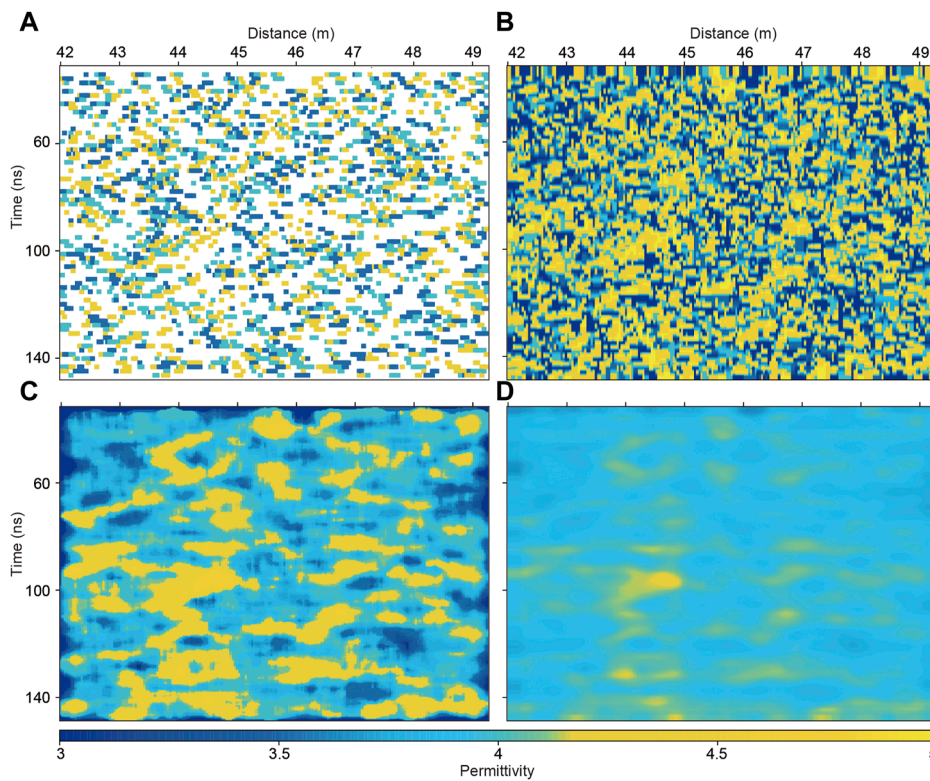


FIGURE 12 Permittivity map obtained from scattering points. (A) The scatter plot of average permittivity. (B) The interpolation result of scattering points shown in (A). (C) The median filtering result of (B). (D) The smoothed map of interval permittivity converted from (C) by Dix inversion.

linear trend from 3.85 to 4.1 between 30 and 150 ns, depicted with the red line in Figure 13A. This indicates that there is almost no rapid variation of permittivity with depth. Furthermore, we calculate the mean and median of permittivity at every moment; after the reservation of only one decimal, we calculate the mode average. As shown in Figure 13B, the statistical curves reemphasize the increasing trend of permittivity *versus* time, and the upward tendency indicated by the mean and median permittivity are basically the same, but the curve of mean value changes more gently. It is also worth noticing that with the increasing of depth, the permittivity varies more violently. This phenomenon indicates that the heterogeneity of lunar regolith would be more obvious in deeper materials, which is generally consistent with the gardening process of shallow lunar materials (Zhang, J, et al., 2021).

Another statistics and error analysis is carried out by averaging the estimated permittivities every 5 time steps, as illustrated in Figure 14A. The time points are marked with red dots, and the one standard deviation (1σ) errors within each subsection are identified with dark bars, indicating the confidence bound of our results. For instance, the average permittivity at time point t_0 is calculated with

$$\epsilon_{r,t_0} = \frac{\sum_{i=t_0-4}^{t_0+4} \epsilon_{r,i}}{9}, t_0 = 5, 10, 15 \dots \tag{15}$$

This graph provides a new sight for analyzing the permittivity distribution. Averaging the permittivity helps to limit the influence of some singular permittivity values while retaining the local

characteristics on the overall trend, which is beneficial to summarize the relationship between permittivity and travel time.

With the estimated permittivity at a certain travel time, we can extract a relationship by curve fitting as

$$\epsilon_r = \frac{4.1t + 16.41}{t + 6.884}, \tag{16}$$

where t is the travel time (ns), ϵ_r is the relative permittivity. Consistent with previous studies, the statistical regulation shows an increasing trend of permittivity *versus* depth, indicating that the relative permittivity of lunar subsurface materials is in strong positive correlations with depth. The red curve in Figure 14B represents the averaged permittivity at every moment, and the blue curve is the fitted relationship. With these fitting results, we can analyze the degree of permittivity variation within this region. The peaks and valleys at time point t_j are collected and the root mean square local permittivity perturbation ξ can be calculated with

$$\xi = \sum_{j=1}^N \frac{|\epsilon_{r,t_j} - \epsilon_{fit,t_j}|}{N \cdot \epsilon_{fit,t_j}}, \tag{17}$$

where N is the number of peaks and valleys, ϵ_{r,t_j} and ϵ_{fit,t_j} is the averaged relative permittivity and the fitted one, respectively. The local permittivity perturbation ξ is estimated to be $\sim 2.3\%$, which is consistent with 3% obtained by the simulated results (Zhang, X., et al., 2021). This verified that the lunar regolith at the Chang'E-4 landing area can be well described by self-organization random models.

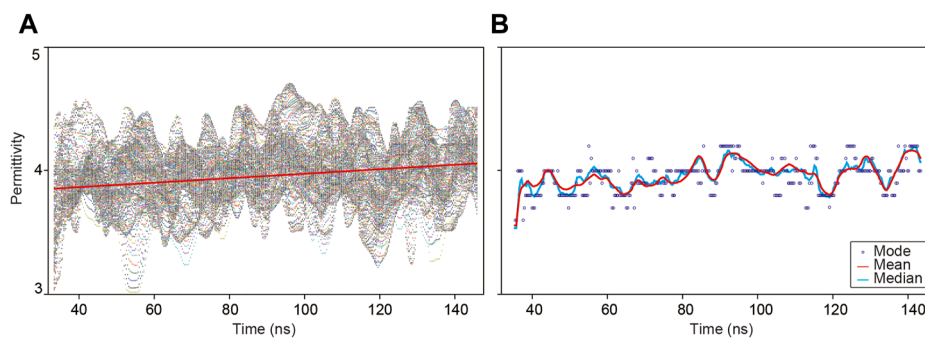


FIGURE 13

Statistical characteristics of permittivity distribution. (A) The scatterplot of permittivity, where the red line is the linear fitting result. (B) The mode, mean and median permittivities at every moment.

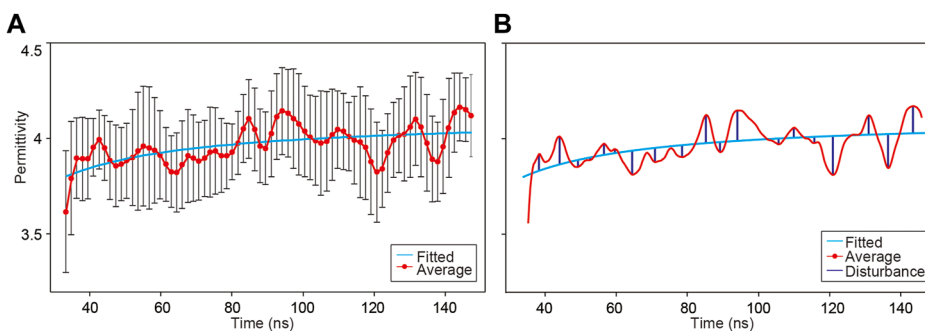


FIGURE 14

Permittivity distribution along time. (A) The red line with dots and the black bars represent the average permittivity and one standard deviation every 5 time steps, respectively. (B) The red line is the average permittivity at every moment, and the blue curve represents the fitting result. The vertical bars represent the perturbation of peaks and valleys.

4 Discussion

Compared with the existing methods, our method has some unique advantages. The hyperbolic-fitting method requires that the diffractions should be in well-formed and distinguishable hyperbolic shape, which is difficult to achieve in practice; additionally, the traditional migration method can not suppress the surrounding noises and interferences in the focusing analysis due to working on the whole profile, which may lead to large errors. Our method combines the advantage of hyperbolic fitting and migration; thus, it can help to estimate the relative permittivity more precisely and effectively, especially for complex materials. Besides, the spatial resolution of our method is to that of the LPR payload, which can help to better recognize and delineate the abnormal bodies in subsurface materials.

Limited by the computation cost, our method is only applied in shallow part within 12 m in depth and within ~ 7 m in distance; however, the statistical characteristics extracted from this local area should be universal to the Chang'E-4 landing area along the rover's track. The map of permittivity distribution shows that there is an abnormal high-permittivity region existing in the map at ~ 100 ns? We suppose that small basaltic or ejecta blocks may gather there. Besides, we can notice that the permittivity becomes larger

and varies severer with the increasing depth. This indicates that there is a strong positive correlation between the permittivity of lunar subsurface materials and depth, and the heterogeneity of lunar regolith is more obvious in deeper materials. The increasing tendency of permittivity with depth is consistent with former studies (Heiken et al., 1991). We suppose this is probably because of more blocks or larger grain size of deeper materials.

5 Conclusion

We propose a migration-based method to estimate the relative permittivity of subsurface materials from the ground penetrating radar data, including three steps: diffraction isolation, migration, and focusing analysis. Single point test shows that diffraction isolation can help to improve the reliability of migration and is a prerequisite for accurate focusing analysis in the migrated domain. Numerical experiments show that the proposed method is robust and effective for permittivity estimation, especially in the presence of strong noises and cluttered diffractions. The spatial resolution is higher than that of the existing methods due to the application of diffraction isolation and migration; thus, we can pick up a great number of diffractors, which is helpful to

construct a continuous velocity profile in depth. The permittivity at the Chang'E-4 landing area is estimated to be ~ 4 within 12 m, ranging from 3.5 to 4.2. Additionally, the local perturbation of the permittivity is $\sim 2.3\%$, which is consistent with that ($\sim 3\%$) obtained by numerical simulations using self-organization random models. This suggests that the lunar regolith at Chang'E-4 landing area is mature and can be well described by the self-organization random models.

Data availability statement

Publicly available datasets were analyzed in this study. This data can be found here: https://moon.bao.ac.cn/ce5web/searchOrder_dataSearchData.search.

Author contributions

Conceptualization: WL and JZ; Methodology: WL; Supervision: JZ; Writing—Original draft: WL and JZ; Writing—Review and editing: WL and JZ. All authors contributed to the article and approved the submitted version.

Funding

This research was supported by the National Natural Science Foundation of China (41941002), Key Research Program of the

Institute of Geology and Geophysics, CAS (IGGCAS-202203), and Key Research Program of the Chinese Academy of Sciences (ZDBS-SSWTLC001). JZ was also supported by Foundation for Excellent Member of the Youth Innovation Promotion Association, Chinese Academy of Sciences (2016).

Acknowledgments

We thank the Supercomputing Laboratory of Institute of Geology and Geophysics, Chinese Academy of Sciences (IGGCAS) for providing computing resources.

Conflict of interest

The authors declare that the research was conducted in the absence of any commercial or financial relationships that could be construed as a potential conflict of interest.

Publisher's note

All claims expressed in this article are solely those of the authors and do not necessarily represent those of their affiliated organizations, or those of the publisher, the editors and the reviewers. Any product that may be evaluated in this article, or claim that may be made by its manufacturer, is not guaranteed or endorsed by the publisher.

References

- Boisson, J., Heggy, E., Clifford, S. M., Frigeri, A., Plaut, J. J., Farrell, W. M., et al. (2009). Sounding the subsurface of Athabasca Valles using MARSIS radar data: Exploring the volcanic and fluvial hypotheses for the origin of the rafted plate terrain. *J. Geophys. Res. Planets* 114 (E8). doi:10.1029/2008JE003299
- Bradford, J. H., and Harper, J. T. (2005). Wave field migration as a tool for estimating spatially continuous radar velocity and water content in glaciers. *Geophys. Res. Lett.* 32 (8), L08502. doi:10.1029/2004GL021770
- Capineri, L., Daniels, D. J., Falorni, P., Lopera, O. L., and Windsor, C. G. (2008). Estimation of relative permittivity of shallow soils by using the ground penetrating radar response from different buried targets. *Prog. Electromagn. Res. Lett.* 2, 63–71. doi:10.2528/PIERL07122803
- Carpentier, S. F., Horstmeyer, H., Green, A. G., Doetsch, J., and Coscia, I. (2010). Semiauto-mated suppression of above-surface diffractions in GPR data. *Geophysics* 75 (6), J43–J50. doi:10.1190/1.3497360
- Carrier, W. D., Olhoeft, G. R., and Mendell, W. (1991). Physical properties of the lunar surface. *Lunar Sourcebook*, 475–594.
- Claerbout, J. F. (1985). *Imaging the earth's interior*. Oxford: Blackwell scientific publications.
- Dai, S., Su, Y., Yuan, X., Feng, J., and Xing, S. (2014). *Lunar regolith structure model and echo simulation for Lunar Penetrating Radar*. IEEE, Proceedings of the 15th International Conference on Ground Penetrating Radar. July 4, 2014, Belgium, IEEE.
- Ding, C., Li, C., Xiao, Z., Su, Y., Xing, S., Wang, Y., et al. (2020). Layering structures in the porous material beneath the Chang'e-3 landing site. *Earth Space Sci.* 7, e2019EA000862. doi:10.1029/2019EA000862
- Dix, C. H. (1955). Seismic velocities from surface measurements. *Geophysics* 20 (1), 68–86. doi:10.1190/1.1438126
- Dong, Z., Fang, G., Zhao, D., Zhou, B., Gao, Y., and Ji, Y. (2020). Dielectric properties of lunar subsurface materials. *Geophys. Res. Lett.* 47 (22), e2020GL089264. doi:10.1029/2020GL089264
- Economou, N., Vafidis, A., Bano, M., Hamdan, H., and Ortega-Ramirez, J. (2020). Ground-penetrating radar data diffraction focusing without a velocity model. *Geophysics* 85 (3), H13–H24. doi:10.1190/geo2019-0101.1
- Fa, W., Zhu, M., Liu, T., and Plescia, J. (2015). Regolith stratigraphy at the Chang'E-3 landing site as seen by lunar penetrating radar. *Geophys. Res. Lett.* 42 (23), 10179–10187. doi:10.1002/2015gl066537
- Fang, G., Zhou, B., Ji, Y., Zhang, Q., Shen, S., Li, Y., et al. (2014). Lunar penetrating radar onboard the chang'e-3 mission. *Res. astronomy astrophysics* 14 (12), 1607–1622. doi:10.1088/1674-4527/14/12/009
- Feng, J., Su, Y., Li, C., Dai, S., Xing, S., and Xiao, Y. (2019). An imaging method for Chang'e5 Lunar Regolith Penetrating Radar. *Planet. Space Sci.* 167 (MAR.), 9–16. doi:10.1016/j.pss.2019.01.008
- Fomel, S., Landa, E., and Taner, M. T. (2007). Poststack velocity analysis by separation and imaging of seismic diffractions. *Geophysics* 72 (6), U89–U94. doi:10.1190/1.2781533
- Fomel, S. (2003a). Time-migration velocity analysis by velocity continuation. *Geophysics* 68 (5), 1662–1672. doi:10.1190/1.1620640
- Fomel, S. (2003b). Velocity continuation and the anatomy of residual prestack time migration. *Geophysics* 68 (5), 1650–1661. doi:10.1190/1.1620639
- Giannakis, I., Zhou, F., Warren, C., and Giannopoulos, A. (2021). Inferring the shallow layered structure at the chang'e-4 landing site: A novel interpretation approach using lunar penetrating radar. *Geophys. Res. Lett.* doi:10.1002/essoar.10506249.1
- Gold, T., Bilson, E., and Yerbury, M. (1972). Grain size analysis, optical reflectivity measurements, and determination of high-frequency electrical properties for Apollo 14 lunar samples. *Lunar Planet. Sci. Conf. Proc.*
- Hamran, S. E., Paige, D. A., Amundsen, H., Berger, T., Yan, M. J., Carter, L., et al. (2020). Radar imager for Mars' subsurface experiment—rimfax. *Space Sci. Rev.* 216 (128), 128. doi:10.1007/s11214-020-00740-4
- Heiken, G. H., Vaniman, D. T., and French, B. M. (1991). *Lunar Sourcebook, a user's guide to the Moon*. Houston, Texas. Cambridge University Press.

- Hiesinger, H., and Head, J. W., III (2006). New views of lunar geoscience: An introduction and overview. *Rev. Mineralogy Geochem.* 60 (1), 1–81. doi:10.2138/rmg.2006.60.1
- Hu, J., Schuster, G. T., and Valasek, P. A. (2001). Poststack migration deconvolution. *Geophysics* 66 (3), 939–952. doi:10.1190/1.1444984
- Jol, H. (2009). *Ground penetrating radar: Theory and applications*. Germany: Elsevier Science.
- Jolliffe, B. L., Wiecek, M. A., Shearer, C. K., and Neal, C. R. (2006). *New views of the Moon*. Beijing: Walter de Gruyter GmbH and Co KG. doi:10.2138/rmg.2006.60.0
- Jordan, R., Picardi, G., Plaut, J., Wheeler, K., Kirchner, D., Safaeinili, A., et al. (2009). The Mars express MARSIS sounder instrument. *Planet. Space Sci.* 57 (14–15), 1975–1986. doi:10.1016/j.pss.2009.09.016
- Kouemou, G. (2010). *Radar technology*. Germany BoD–Books on Demand.
- Leong, Z. X., and Zhu, T. (2021). Direct velocity inversion of ground penetrating radar data using GPRNet. *J. Geophys. Res. Solid Earth* 126, e2020JB021047. doi:10.1029/2020JB021047
- Leuschen, C. J., and Plumb, R. G. (2001). A matched-filter-based reverse-time migration algorithm for ground-penetrating radar data. *IEEE Trans. Geoscience Remote Sens.* 39 (5), 929–936. doi:10.1109/36.921410
- Li, C., Lin, Y., Lv, W., and Zhang, J. (2021b). Eliminating above-surface diffractions from ground-penetrating radar data using iterative Stolt migration. *Geophysics* 86 (1), H1–H11. doi:10.1190/GEO2019-0796.1
- Li, C., Zhang, J., Loxas, M., and Sharma, P. (2021a). Hemosiderotic dermatofibroma mimicking melanoma: A case report and review of the literature. *Remote Sens.* 13, 1387–1392. doi:10.3390/rs13071387
- Li, C., and Zhang, J. (2022a). Preserving signal during random noise attenuation through migration enhancement and local orthogonalization. *Geophysics* 87, V451–V466. doi:10.1190/geo2021-0385.1
- Li, C., and Zhang, J. (2022b). Wavefield separation using irreversible-migration filtering. *Geophysics* 87 (3), A43–A48. doi:10.1190/GEO2021-0607.1
- Li, C., Zheng, Y., Wang, X., Zhang, J., Wang, Y., Chen, L., et al. (2022). Layered subsurface in utopia basin of Mars revealed by zhurong rover radar. *Nature* 610, 308–312. doi:10.1038/s41586-022-05147-5
- Li, J., Zeng, Z., Liu, C., Huai, N., and Wang, K. (2017). A study on lunar regolith quantitative random model and lunar penetrating radar parameter inversion. *IEEE Geoscience Remote Sens. Lett.* 14 (11), 1953–1957. doi:10.1109/LGRS.2017.2743618
- Lv, W., Li, C., Song, H., Zhang, J., and Lin, Y. (2020). Comparative analysis of reflection characteristics of lunar penetrating radar data using numerical simulations. *Icarus* 350, 113896. doi:10.1016/j.icarus.2020.113896
- Olhoeft, G., Frisillo, A., Strangway, D., and Sharpe, H. (1974). Temperature dependence of electrical conductivity and lunar temperatures. *moon* 9 (1-2), 79–87. doi:10.1007/bf00565394
- Olhoeft, G. R., and Strangway, D. W. (1975b). Dielectric properties of the first 100 meters of the Moon. *Earth Planet. Sci. Lett.* 24, 394–404. doi:10.1016/0012821x(75)90146-6
- Olhoeft, G., Strangway, D., and Pearce, G. (1975a). Effects of water on electrical properties of lunar fines. *Proc. Lunar Sci. Conf.* 6th, 3333–3342.
- Oudart, N., Ciarletti, V., Le Gall, A., Mastrogiuseppe, M., Hervé, Y., Benedix, W. S., et al. (2021). Range resolution enhancement of WISDOM/ExoMars radar soundings by the Bandwidth Extrapolation technique: Validation and application to field campaign measurements. *Planet. Space Sci.* 197, 105173. doi:10.1016/j.pss.2021.105173
- Özdemir, C., Demirci, Ş., Yiğit, E., and Yilmaz, B. (2014). A review on migration methods in B-scan ground penetrating radar imaging. *Math. Problems Eng.* 2014, 1–16. doi:10.1155/2014/280738
- Reshef, M., and Landa, E. (2009). Post-stack velocity analysis in the dip-angle domain using diffractions. *Geophys. Prospect.* 57 (5), 811–821. doi:10.1111/j.1365-2478.2008.00773.x
- Ristic, A. V., Petrovacki, D., and Govedarica, M. (2009). A new method to simultaneously estimate the radius of a cylindrical object and the wave propagation velocity from GPR data. *Computers and Geosciences* 35 (8), 1620–1630. doi:10.1016/j.cageo.2009.01.003
- Roquette, P., Gattacceca, J., Ivanov, A., Nazarov, M., and Bezaeva, N. (2010). Magnetic properties of lunar materials: Meteorites, Luna and Apollo returned samples. *Earth Planet. Sci. Lett.* 292 (3–4), 383–391. doi:10.1016/j.epsl.2010.02.007
- Sato, M., and Feng, X. (2005). *GPR migration algorithm for landmines buried in inhomogeneous soil*. *IEEE Antennas and Propagation Society International Symposium*.
- Sava, P. C., Biondi, B., and Etgen, J. (2005). Wave-equation migration velocity analysis by focusing diffractions and reflections. *Geophysics*, 70(3), U19–U27. doi:10.1190/1.1925749
- Schroeder, D. M., Dowdeswell, J. A., Siegert, M. J., Bingham, R. G., Chu, W., MacKie, E. J., et al. (2019). Multidecadal observations of the Antarctic ice sheet from restored analog radar records. *Proc. Natl. Acad. Sci.* 116 (38), 18867–18873. doi:10.1073/pnas.1821646116
- Soldovieri, F., and Solimene, R. (2010). Ground penetrating radar subsurface imaging of buried objects. *Tech.*
- Song, H., Li, C., Zhang, J., Wu, X., Liu, Y., and Zou, Y. (2021). Rock location and property analysis of lunar regolith at Chang'E-4 landing site based on local correlation and semblance analysis. *Remote Sens.* 13 (1), 48. doi:10.3390/rs13010048
- Stolt, R. H. (1978). Migration by fourier transform. *Geophysics* 43 (1), 23–48. doi:10.1190/1.1440826
- Stuart, G. (2003). Characterization of englacial channels by ground-penetrating radar: An example from austre Brøggerbreen, Svalbard. *J. Geophys. Res. Solid Earth* 108 (B11), 2525. doi:10.1029/2003JB002435
- Su, Y., Fang, G. Y., Feng, J. Q., Xing, S. G., Ji, Y. C., Zhou, B., et al. (2014). Data processing and initial results of Chang'E-3 lunar penetrating radar. *Res. Astronomy Astrophysics* 14 (12), 1623–1632. doi:10.1088/1674-4527/14/12/010
- Xiao, L., Zhu, P., Fang, G., Xiao, Z., Zou, Y., Zhao, J., et al. (2015). A young multilayered terrane of the northern Mare Imbrium revealed by Chang'E-3 mission. *Science* 347 (6227), 1226–1229. doi:10.1126/science.1259866
- Yilmaz, Ö. (2001). *Seismic data analysis: Processing, inversion, and interpretation of seismic data*. fm: Society of exploration geophysicists. doi:10.1190/1.9781560801580
- Yuan, H., Montazeri, M., Looms, M. C., and Nielsen, L. (2019). Diffraction imaging of ground-penetrating radar data. *Geophysics* 84 (3), H1–H12. doi:10.1190/geo2018-0269.1
- Zhang, H., Zheng, L., Su, Y., Fang, G., Zhou, B., Feng, J., et al. (2014). Performance evaluation of lunar penetrating radar onboard the rover of CE-3 probe based on results from ground experiments. *Res. Astronomy Astrophysics* 14 (12), 1633–1641. doi:10.1088/1674-4527/14/12/011
- Zhang, J., Yang, W., Hu, S., Lin, Y., Fang, G., Li, C., et al. (2015). Volcanic history of the Imbrium basin: A close-up view from the lunar rover Yutu. *Proc. Natl. Acad. Sci.* 112 (17), 5342–5347. doi:10.1073/pnas.1503082112
- Zhang, J., Zhou, B., Lin, Y., Zhu, M., Song, H., Dong, Z., et al. (2021). Lunar regolith and substructure at Chang'E-4 landing site in South Pole-Aitken basin. *Nat. Astron.* 5, 25–30. doi:10.1038/s41550-020-1197-x
- Zhang, X., Lv, W., Zhang, L., Zhang, J., Lin, Y., and Yao, Z. (2021). Self-organization characteristics of lunar regolith inferred by Yutu-2 lunar penetrating radar. *Remote Sens.* 13, 3017. doi:10.3390/rs13153017
- Zhou, B., Shen, S., Lu, W., Liu, Q., Tang, C., Li, S., et al. (2020). The Mars rover subsurface penetrating radar onboard China's Mars 2020 mission. *Earth Planet. Phys.* 4 (4), 1–10. doi:10.26464/epp2020054
- Zhu, J., Lines, L., and Gray, S. (1998). Smiles and frowns in migration/velocity analysis. *Geophysics* 63 (4), 1200–1209. doi:10.1190/1.1444420